



Open-source, cost-effective, portable, 3D-printed digital lensless holographic microscope

HEBERLEY TOBON-MAYA, SAMUEL ZAPATA-VALENCIA, ERICK ZORA-GUZMÁN,
CARLOS BUITRAGO-DUQUE, AND JORGE GARCIA-SUCERQUIA*

School of Physics, Universidad Nacional de Colombia—Sede Medellin, A.A: 3840, Medellin 050034, Colombia

*Corresponding author: jigarcia@unal.edu.co

Received 19 August 2020; revised 16 October 2020; accepted 17 October 2020; posted 20 October 2020 (Doc. ID 405605);
published 17 November 2020

In this work, the design, construction, and testing of the most cost-effective digital lensless holographic microscope to date are presented. The architecture of digital lensless holographic microscopy (DLHM) is built by means of a 3D-printed setup and utilizing off-the-shelf materials to produce a DLHM microscope costing US\$52.82. For the processing of the recorded in-line holograms, an open-source software specifically developed to process this type of recordings is utilized. The presented DLHM setup has all the degrees of freedom needed to achieve different fields of view, levels of spatial resolution, and 2D scanning of the sample. The feasibility of the presented platform is tested by imaging non-bio and bio samples; the resolution test targets, a section of the head of a *Drosophila melanogaster* fly, red blood cells, and cheek cells are imaged on the built microscope. © 2020 Optical Society of America

<https://doi.org/10.1364/AO.405605>

1. INTRODUCTION

Simple and affordable 3D-printing systems have driven the development of cost-effective, portable, and lightweight devices in different fields of science and technology. In particular, the field of microscopy has been greatly benefited because 3D printers have made it possible to achieve cost-effective, compact, robust, field-portable, and lightweight imaging systems with high throughput for different modalities of microscopy. From the very large list of 3D-printed microscopes, one can start by mentioning the OpenFlexure project [1]. This 3D-printed microscope is based on a regular microscope objective, a tube lens, and an 8MP CMOS sensor (Raspberry Pi camera V2) to offer different microscopy modes of operation; bright-field trans-illumination, bright-field epi-illumination, polarization-contrast imaging, and fluorescence imaging are the modalities in which this microscope can operate. However, because of the utilized imaging principle, it is not possible to make quantitative imaging of transparent samples in this system. To this aim, the 3D-printed microscope should resort to mainly interferometric principles of microscopic imaging [2].

There are different modalities of microscopes based on interferometric principles that have been developed using 3D-printing technology. Initially, one could mention those based on off-axis digital holographic microscopy [3]. In general, this methodology needs to record the interference of two waves with a given degree of inclination between them. The fringe pattern resulting from this amplitude superposition constitutes the carrier information that is modulated by the imaged sample. The recovery of the sample information, both in amplitude and

phase, can be done by a regular spatial filtering approach [4,5]. Currently, off-axis 3D-printed digital holographic microscopes based on the interference of two point-sources [6,7], on side illumination and analog hologram gratings [8], on shearing digital holography [9,10], and on slide holographic microscopy [11] are available.

An alternative option for interferometric imaging in microscopy is the in-line configuration [12]. In this configuration, the information of the sample is gathered by the propagation of the illuminating wavefront through the micrometer-sized specimen. The minimum needed components for the architecture of in-line holographic microscopy are an illumination source and a digital recording device. When the illumination is provided by a point source, the recorded intensity can be understood as a magnified diffraction pattern from which the information of the specimen can be somehow retrieved. This simplicity of hardware sets the digital in-line holographic microscopy architecture as a noteworthy candidate to the production of compact, robust, cost-effective, and 3D-printed digital holographic microscopes. Indeed, numerous developments that take advantage of this architecture can be found in the literature. Some of the earliest reports on cost-effective digital holographic microscopes based on the in-line architecture come from Ozcan's group [13–16]. In these works, Ozcan proposed the use of point-source illumination with the sample very close to the digital camera to achieve, employing multiple shots and intensive computational effort, an enormous field of view of around 8 cm², and micrometer-sized spatial resolution. Another set of notable works of digital in-line holographic microscopy that reported

compact and cost-effective setups can be read in [17,18]; in these references, the building price ranges from US\$1000 to US\$250, and the reported spatial resolutions are about 3 μm . Further development in this direction, explicitly including the use of substantially cost-effective light sources, was reported by Micó's group [19,20]. In this multiframe single-shot in-line architecture, micrometer-sized spatial resolution and observation of dynamic events are reported. Following the path to push for price reduction in making digital in-line holographic microscopes, researchers of the Institute of Applied Physics at Technische Universität Darmstadt in Germany have presented an open-source 3D-printed digital in-line holographic microscope for low-cost cellular imaging [21]. In this work, the researchers use laser diode and LED illumination to offer two different microscopes with a varied optical performance. For the geometry of their microscopes, the nominal field of view and spatial resolution is fixed, yielding the spatial resolution controlled by the light source; while for the laser diode a spatial resolution of 1.55 μm is obtained, for the LED illumination 3.91 μm is claimed. The price reported for the making of the LED-based digital in-line holographic microscope, the less expensive of the two, is US\$190.

In the present work, the design, construction, and testing of an open-source, cost-effective, portable, 3D-printed digital lensless holographic microscope, are reported. The presented microscope is based on the digital lensless holographic microscopy (DLHM) [22–24] technology. DLHM is a digital in-line holographic microscopy technique that provides micrometer-sized spatial resolution by using spherical wavefront illumination light sources with numerical apertures above 0.4. The proposed open-source, cost-effective, portable, 3D-printed digital lensless holographic microscope offers the full set of degrees of freedom to vary the field of view of the microscope at different levels of spatial resolution. For the easy 2D scanning of the sample, the body of the microscope has been equipped with a slide holder. As compared with the most cost-effective digital holographic microscope to date [21], the one presented in this work is almost 4 times less expensive, provides full access to a varying field of view and spatial resolution, and provides accurate 2D scanning of the sample. A fully open-source processing software joins the 3D-printed microscope to access the said optical features from software. The capabilities of the constructed open-source, cost-effective, portable, 3D-printed digital lensless holographic microscope have been tested on imaging resolution test targets, a section of the head of a *Drosophila melanogaster*, red blood cells, and cheek cells.

2. FUNDAMENTALS

DLHM [22–24] is a realization of the original invention of Gabor's invention [25] with modern technology. A point source illuminates a weakly scattering sample placed at a distance z from the said source. A digital camera, located L apart from the point source, records the intensity resulting from the diffraction of the spherical wavefronts emitted by the point source on the sample. Figure 1 illustrates a DLHM setup.

The diffraction pattern, known as in-line hologram, is magnified by the free-space propagation from the sample to the digital camera. The value of such magnification $M = L/z$ must be such

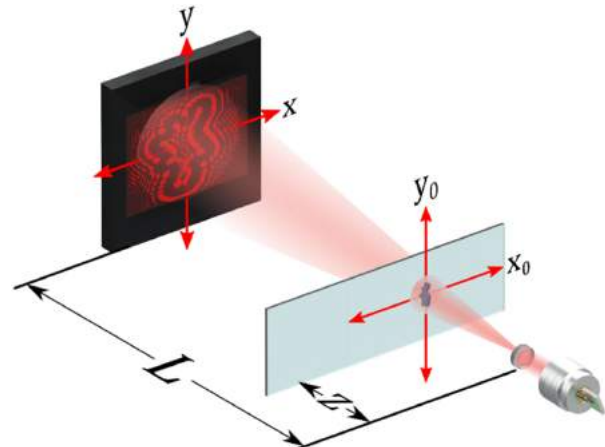


Fig. 1. Illustration of the recording setup of a digital lensless holographic microscope.

that the recording of the in-line hologram fulfills the sampling requirements [26,27]. Also, the value of M can be utilized to categorize the two types of microscopy without lenses [16,19,20]: while $M < 1$, the sample close to the digital camera, denotes what is mainly known as computational microscopy [28–30], values of $M > 1$, the sample close to the point source, apply for methods of lensless microscopy such as multi-illumination single-holographic-exposure lensless Fresnel (MISHELF) [19,31,32] or DLHM [24,33,34]. As inherited from Gabor's idea of holography, the very first understanding of the in-line hologram of DLHM is modeled as the amplitude superposition of a reference $U_{\text{ref}}(\vec{r})$ with an object wave $U_{\text{scat}}(\vec{r})$ on the plane of the digital camera, where the position vector $\vec{r} = (x, y, L)$ is measured from the point source to denote a point on the digital camera plane. The former is the portion of the spherical wave that propagates from the point source to the digital camera with no perturbation, regularly assumed to be the diverging spherical wave that illuminates the sample $U_{\text{ref}}(\vec{r}) = \exp[ik\vec{r}]/|\vec{r}|$; the object wave is the portion of the spherical wavefront that, after undergoing a diffraction process on the sample, propagates to the said digital camera. In this framework, the in-line hologram can be read as

$$\begin{aligned} I(\vec{r}) &= [U_{\text{ref}}(\vec{r}) + U_{\text{scat}}(\vec{r})] [U_{\text{ref}}(\vec{r}) + U_{\text{scat}}(\vec{r})]^* \\ &\approx U_{\text{ref}}(\vec{r}) U_{\text{ref}}^*(\vec{r}) + U_{\text{ref}}(\vec{r}) U_{\text{scat}}^*(\vec{r}) + U_{\text{ref}}^*(\vec{r}) U_{\text{scat}}(\vec{r}). \end{aligned} \quad (1)$$

In Eq. (1), the $*$ superscript denotes the complex conjugate, and the intensity of the object wave $U_{\text{scat}}(\vec{r}) U_{\text{scat}}^*(\vec{r})$ is negligible, as for DLHM to work the sample must be a weak scatterer [25]. The first term of the equation corresponds to the intensity of the reference wave, and the last two terms are the twin images, whose effects on the performance of DLHM can be read elsewhere [24,35].

Upon the understanding that in the DLHM architecture it is not possible to have a reference wave fairly described as a diverging spherical wavefront, an alternative model for the in-line hologram based on a simple diffraction phenomenon has been proposed [34,36]. The recorded in-line hologram is, therefore, the resulting single-shot intensity of the diffraction process that

undergoes a diverging spherical wavefront $\exp[ik\vec{r}]/|\vec{r}|$ and the sample with a given transmittance $S(\vec{r}_0)$. With the sample placed at a distance z from the point source that produces the diverging spherical wavefront, the in-line hologram can be correctly described through the Rayleigh–Sommerfeld diffraction formula [26] as

$$I(\vec{r}) = \left| \int_{\text{Sample}} S(\vec{r}_0) \frac{\exp[ik\vec{r}_0]}{|\vec{r}_0|} \frac{\exp[ik(\vec{r} - \vec{r}_0)]}{|\vec{r} - \vec{r}_0|} d\vec{r}_0 \right|^2. \quad (2)$$

In Eq. (2), $|\bullet|^2 = (\bullet)(\bullet)^*$, the position vector $\vec{r}_0 = (x_0, y_0, z)$ denotes a point on the sample plane measured from the point source, $i = \sqrt{-1}$, and $k = 2\pi/\lambda$ is the wavenumber with λ the illumination wavelength.

In either representation, Eq. (1) or Eq. (2), the in-line hologram is a single-shot intensity recorded in the digital camera with a magnification factor of $M = L/z$. From the said magnified intensity, the complex-valued wavefield scattered by the sample can be recovered in the experiment volume contained from the point source to the digital camera. The different planes within this recovering volume are composed of points denoted by position vectors $\vec{r}_r = (x_r, y_r, z_r)$, such that $z \leq z_r \leq L$; the retrieved complex-value wavefield for $z_r = z$ corresponds to the in-focus image of the sample transmittance.

The use of a digital camera to record the in-line hologram provides DLHM with the power and versatility of the digital world. The recovery of the complex-valued wavefield scattered by the sample can be done by means of a fully numerical approach. The recorded in-line hologram $I(\vec{r})$ is pixelwise multiplied by a converging spherical wavefront $\exp[-ik\vec{r}]/|\vec{r}|$, and the complex-valued wavefield resulting from this multiplication is propagated towards the reconstruction plane. This propagation is computed by evaluating the diffraction process of the converging spherical wavefront as it illuminates the in-line hologram. This process can be numerically described by means of a scalar diffraction formula [26]:

$$U(\vec{r}_r) = \int_{\text{Digital Camera}} I(\vec{r}) \frac{\exp[-ik\vec{r}]}{|\vec{r}|} \frac{\exp[-ik(\vec{r} - \vec{r}_r)]}{|\vec{r} - \vec{r}_r|} d\vec{r}. \quad (3)$$

When $\vec{r}_0 = \vec{r}_r$, the complex-valued wavefield resulting from Eq. (3) represents the wavefield scattered by the sample. From it, one can compute its intensity $U(\vec{r}_0)U^*(\vec{r}_0)$ or phase $\phi(\vec{r}_0) = \arctan(\text{Im}[U(\vec{r}_0)]/\text{Re}[U(\vec{r}_0)])$, with Im and Re being the imaginary and real parts, respectively. As said before, Eq. (3) can be computed for different values of \vec{r}_r within the experiment volume to produce a stack of reconstructed images that could be used to produce a 3D recreation of the sample volume, within the axial resolution limits of DLHM [24]. The numerical implementation of Eq. (3) follows a coordinate remapping and change of variables proposed by Kreuzer, aimed to cast this equation into a fast Fourier transform formalism; the detailed process is described in [35].

As in any other microscopy system, the precise control of the spatial resolution and the field of view (FOV) is essential. The spatial resolution in DLHM and related methods has been extensively studied [24,37–41]. For the practical interest of the present work, one can state that two point objects can be

distinguished in DLHM if the distance between them Δr is such that

$$\Delta r \geq \frac{\lambda}{2NA}. \quad (4)$$

In Eq. (4) NA is the effective numerical aperture, which is taken to be the smallest between that of the illuminating point source and that of the recording setup. The NA of the illuminating point source is set by the method used to produce the said source. Conventionally in DLHM, the point source is produced by focusing down the light of a laser onto the surface of a metallic pinhole with a diameter in the order of λ , to render to a maximum illuminating NA of 0.77 [24]; however, alternative developments have been proposed with engineered optical fibers to produce point sources valid for DLHM with NA of 0.88 [42,43]. Similarly, the NA of the recording setup of DLHM is given by the geometry of the arrangement

$$NA = \frac{W}{2\sqrt{(\frac{W}{2})^2 + L^2}} \quad (5)$$

with W the width of the digital camera. In the common practice of DLHM, the NA of the illuminating point source is set up as the upper limit. Hence, the effective NA of the DLHM microscope is usually the one given by the geometry of the recording arrangement, provided that it is always smaller than the one of the illuminating point source.

The FOV of the DLHM microscope is also controlled by the geometry of the recording setup. Upon the condition stated in the last paragraph, imposing the condition that a full illumination of the width W of the camera must be guaranteed, the FOV of DLHM is a circle whose area is given by

$$\text{FOV} = \pi \left(\frac{Wz}{2L} \right)^2. \quad (6)$$

In summary, Eq. (5) and Eq. (6) state that a DLHM microscope could operate at all the theoretically available ranges of spatial resolution and FOV, only if the distances between the point source and the sample and between the point source and the digital camera can be varied independently. This crucial condition has been considered in the design and construction of the open-source, cost-effective, 3D-printed DLHM to be presented in the sections to follow.

3. DESIGN AND CONSTRUCTION OF THE OPEN SOURCE, COST-EFFECTIVE, 3D-PRINTED DLHM

The recognized parameters of the DLHM architecture that determine its performance were taken into account to drive an open-source, cost-effective, and 3D-printable design of a DLHM microscope. The point source, the digital camera, the body of the microscope, and the processing software are the elements that were integrated in a coordinated way to produce a design that can fulfill the expected features in terms of open reproducibility, price, and manufacturability.

A. Point-Source Module

The point source has been recognized as a key element in the overall performance of the DLHM microscopes [34,42,43] and similar architectures [19]. As stated before, in conventional DLHM microscopes, the point source is produced by focusing down the light from a laser or a LED upon the surface of a metallic pinhole with a diameter in the order of the illuminating wavelength. This method, which can produce point sources with $\text{NA} = 0.77$ at most [24], is highly demanding in the required optomechanics, leading to a costly and bulky source with limited mechanical stability [34]. As a response to these unwanted features for a key element of the DLHM microscopes, different options have been explored. Optical pick-up units, particularly those for Blu-ray technology [44], can produce writing/reading spots with a diameter in the order of 300 nm, which, for an illuminating wavelength of 405 nm, imposes $\text{NA} \approx 0.85$. This figure sets the optical pick-ups as a desirable point source for DLHM or related architectures [19]; however, the reverse engineering needed for its appropriate use hinders a wide range of applications. A very attractive point source for DLHM, supported on engineered optical fibers, has also been developed [34,42,43]; nonetheless, despite the outstanding results achievable with this also cost-effective point source, this development presently lacks the mechanical robustness needed for being the most solid candidate for the point source of DLHM.

Gradient-index (GRIN) lenses [45] and aspheric lenses [20] have also been presented as alternative methods for producing point sources. The former exhibits an excellent optical performance with a reasonable NA, but its price and the needed fine optomechanics for its assembly conceal the possibility of them being utilized in the present work. Aspheric lenses are also available at a wide range of NA, but at a much lower entry price, with easy optomechanical implementation and the possibility of being purchased as a plug-and-play device to be coupled with cost-effective laser diodes; these characteristics rank the aspheric lenses as the most appropriate element to produce a cost-effective, robust, and easy-to-assemble point-source module for DLHM.

Figure 2 shows a 3D rendering of the point source developed for the present microscope. A 5 mW laser diode, costing US\$1.03 and operating at 4 VDC, shines 650 nm light; see ① in Fig. 2. The laser light is collected by a $\text{NA} = 0.65$ plug-and-play aspheric lens ②, with a cost of US\$4.70; this price includes the retaining holders denoted by ③ in Fig. 2. The laser diode with the assembled aspheric lens is hosted in the 3D-printed housing indicated by ④ in Fig. 2. An effective $\text{NA} = 0.65$ of the built point source was measured following the regular procedure proposed by Mandel *et al.* [46], which assumes a Gaussian beam propagation. According to this method, the NA is related to the change of the full width at half-maximum (FWHM) along a propagation distance ΔZ by

$$\text{NA} = \sin \left[\tan^{-1} \left(\frac{\Delta \text{FWHM}}{\sqrt{2 \ln 2} \Delta Z} \right) \right], \quad (7)$$

where the FWHM is related to the radius of the beam's spot $w(Z)$ at a distance Z from the aspherical lens by

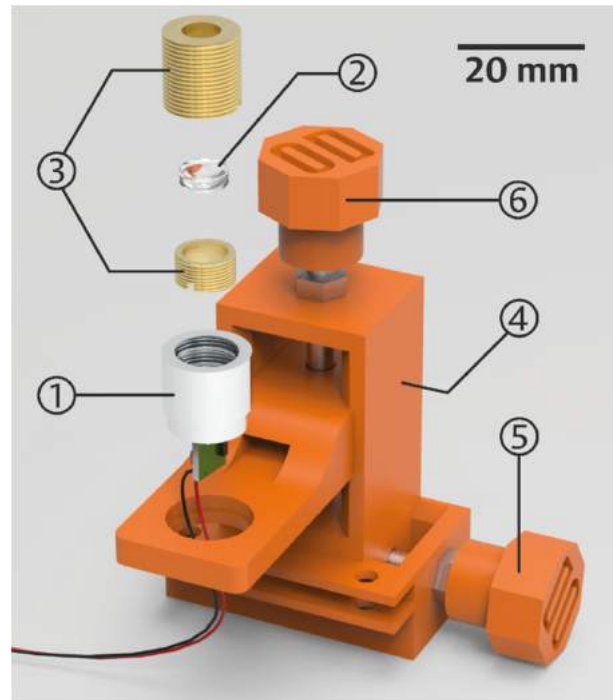


Fig. 2. Point source module for DLHM based on an aspheric lens. ① Laser diode. ② Aspheric lens. ③ Retaining holders. ④ 3D-printed housing. ⑤ Alignment screw. ⑥ Distance control screw.

$$w(Z) = \frac{\text{FWHM}}{\sqrt{2 \ln 2}}. \quad (8)$$

In summary, the point-source module developed for this DLHM microscope has a $\text{NA} = 0.65$, allows its alignment with screw ⑤ in Fig. 2, and sets its distance to the sample with screw ⑥ in the same figure. The total cost of the designed and built point source is US\$5.79.

B. Digital Camera Module

One of the most expensive materials to build a lensless microscope is the digital camera. In the case of computational microscopy [16], digital cameras with a sensitive area in the order of 8 cm^2 are used to have a FOV in that same order. In DLHM and related architectures [24,32], scientific-grade digital cameras at board level are regularly utilized. In both cases, the cost of these cameras is above the US\$1000 mark.

With the aim of developing a cost-effective DLHM microscope, a surveillance camera manufactured by ELP (ELP-USB500W05G-FD100), shown as ① in Fig. 3, is used for the recording of the in-line holograms. This camera has 2592×1944 square pixels with $2.2 \mu\text{m}$ of side length; however, to prevent anisotropies in the parametrization of the system, the sensing area can be cropped to its lower limit of 1944×1944 pixels. These dimensions of the sensitivity area indicate that, for the given $\text{NA} = 0.65$ of the built point source, the minimum distance point-source camera that can be utilized is 2.5 mm. This board-level camera has hardware dimensions of $38 \text{ mm} \times 38 \text{ mm}$. A 3D-printed housing, shown as ② in Fig. 3, is attached to two screws, marked as ③ and ④ in the same

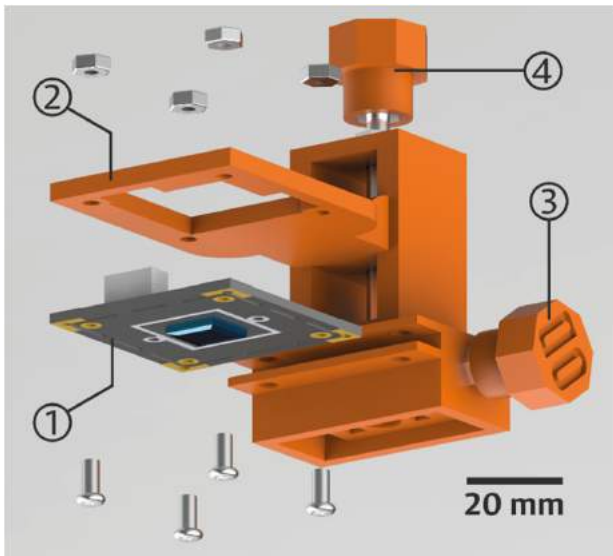


Fig. 3. Digital camera module. ① Digital camera. ② 3D-printed housing. ③ Alignment screw. ④ Height control screw.

figure, that allow the alignment and the height control, in that order; the operation of these screws is detailed in the body of the DLHM microscope section. The cost of the chosen digital camera for this work is US\$43.04.

C. Body of the DLHM Microscope

Figure 4 shows the designed and 3D-printed body of the DLHM microscope and the point-source and digital camera modules; see ①, ②, and ③ in Fig. 4. The design of the body of the DLHM microscope was done considering all the needed degrees of freedom to make mechanically accessible the limit FOV and spatial resolution dictated by the produced point source and the assembled digital camera. To this aim, the modules attached to the body of the microscope have been equipped with the screws ④ and ⑤. Each of these screws has a 19 mm total travel along the z direction; therefore, the point-source-to-sample distance can be varied from 0 to 19 mm, and the point-source-to-digital-camera distance from 2.5 to 21.5 mm. For the limiting $NA = 0.65$ set by the built point source, the body of the microscope offers to the user a FOV from 0.023 to 11.24 mm 2 and a spatial resolution from 0.5 to 6.5 μm . For the alignment of the DLHM, an imaginary line perpendicular to the center of the digital camera must cross by the center of the spherical lens, where the point source is produced. To do this alignment, the body of the microscope is also equipped with the screws ⑥ in Fig. 4. The stage of the microscope, marked as ⑦ in Fig. 4, has 50 cm 2 to allow the free and controlled displacement of the microscope slide. This $x - y$ displacement is done through the spring-loaded slide holder, shown as ⑧ in Fig. 4, which offers a travel distance of 7.1 mm along the x axis and 15 mm along the y axis.

The assembled body of the presented DLHM microscope weights less than 280 grams, and the 102 grams of polylactic acid (PLA) needed for its printing cost approximately US\$1.60.

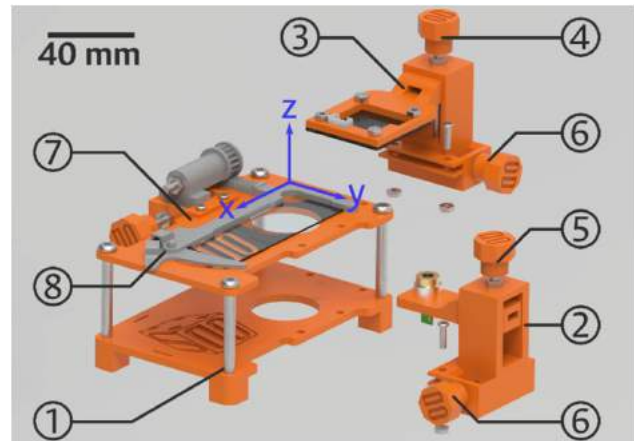


Fig. 4. 3D-printed body of the DLHM microscope. ① Microscope body. ② Point source module. ③ Digital camera module. ④ Screw to change the height of the camera. ⑤ Screw to control de distance of the point source. ⑥ Alignment screws. ⑦ Stage of the microscope. ⑧ Slide holder.

D. Processing Software

The processing of the recorded in-line holograms is done with an open-source ImageJ [47] plugin developed in our group [36]; Fig. 5 shows the graphical user interface of the developed plugin. In group ① of the controls, the user sets up the parameters to perform the reconstruction of the in-line hologram; the names of the images for the hologram and reference can be chosen in the first two drop-down lists. The wavelength, reconstruction distance, distance from the point source to the camera, and dimensions of the hologram are introduced in the following entry boxes, in that order. The selected parameters are logged into the text field shown in ② of Fig. 5. The processing software offers the user the option of choosing, with the check boxes in group ③ of controls, the type of reconstruction performed, namely, phase, amplitude, intensity, and real or imaginary part of the complex-valued reconstructed wavefield. Group ④ of the controls in Fig. 5 offers the opportunity of running batch reconstructions, moving between reconstruction distances with a fixed step, and changing the plugin settings, which include the input units, the type of scaling for the results, the type of

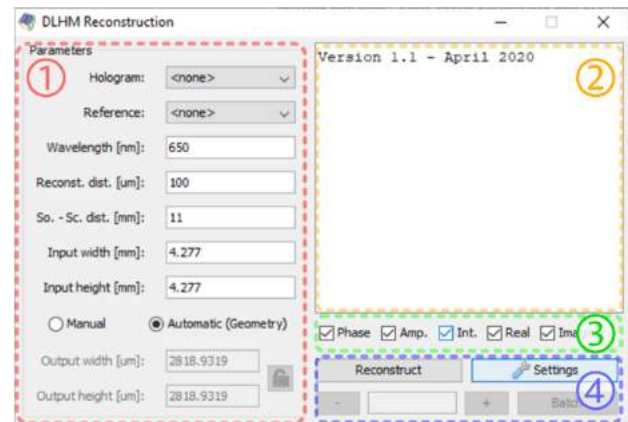


Fig. 5. Graphical user interface of the reconstruction software for the in-line holograms.

optional preprocessing filtering, and many other useful parameters that provide the user with the tools to produce results according to their specific needs. Additionally, the fact that this plugin has been developed for the solid environment of the image processing software of ImageJ [47] powers the processing of the in-line holograms with the full set of useful built-in tools for the representation of the obtained results; for instance, 3D-rendering with a wide set of tunable features like the ones used in this paper. For a complete and detailed description of the processing software, the reader is referred to [36].

4. RESULTS

Following the described design and construction guidelines, a real picture of the manufactured microscope is shown in Fig. 6. The resulting device measures $148.8\text{ mm} \times 112.3\text{ mm} \times 121.6\text{ mm}$ ($\text{W} \times \text{L} \times \text{H}$) and weighs less than 300 grams; it has an imaging system composed of a 650 nm laser illumination collected by a $\text{NA} = 0.65$ aspherical lens and projected into a CMOS camera with a sensing area of 1944×1944 square pixels of $2.2\text{ }\mu\text{m}$ of side length. The microscope has freedom of movement in both the illumination and camera position, allowing adaptation of the FOV and resolution values to the conditions that best suit each specific use case. However, the current implementation does not achieve a complete use of the designed usability ranges; instead, the travel range of the illumination source had to be restricted to stop 2 mm away from the sample stage due to undesirable distortions of the wavefront produced by the aspherical lens in the closest distances. This change limits the maximum achievable resolution and FOV, offering the user an effective FOV from 0.023 to 10 mm^2 and an effective spatial resolution ranging from 1.15 to $6.3\text{ }\mu\text{m}$.

The differences from the experimental values to the design ones are due to the compensation required to prevent distortions from the aspherical lens used as the illumination



Fig. 6. Picture of the open-source, cost-effective, 3D-printed DLHM microscope.

source and mechanical differences in the resulting 3D-printed device. These impasses, especially the aspherical illumination distortions near its focal plane, require further research and development that fall beyond the scope of the present work. Nonetheless, the proposed and constructed microscope is capable of producing high-quality images of microscopic objects, even pure-phase ones, at the lowest cost available in the literature for such a system.

To test the performance of the open-source, cost-effective, 3D-printed DLHM microscope, spatial resolution and FOV evaluations were done over intensity and phase reconstructions using standardized test targets and a biological sample. To improve the visualization of the results, two recordings were made in each case: one with the diffraction pattern of the sample illuminated by the spherical wavefront, as described in Eqs. (1) and (2), and one with the irradiance distribution of the illuminating wavefront without the sample present. The intensity reconstructions were obtained by backpropagating the contrast hologram, which is calculated as the pointwise difference between the two aforementioned recordings; from Eq. (1), it follows that this subtraction removes the $U_{\text{ref}}(\vec{r})U_{\text{ref}}^*(\vec{r})$ term that would otherwise introduce a constant value into the reconstructed field. Similarly, for the phase reconstructions, the recovered fields were divided by the backpropagation of their corresponding reference before computing the phase map; this operation, which is equivalent to the pointwise subtraction of the associated phases, allows compensation of the phase distortion introduced by the carrier wavefront. All these operations, and all the needed processing for the reconstruction of the experimental results, were done with the cited open-source ImageJ plugin and the associated software tools of this same image processing software [36].

A. Spatial Resolution

The evaluation of the spatial resolution of the built microscope was done by imaging a star test target with a nominal height of 150 nm and a USAF 1951 resolution target with a nominal height of 350 nm. Both samples are made of acrylate polymer on glass, allowing them to be considered pure phase objects

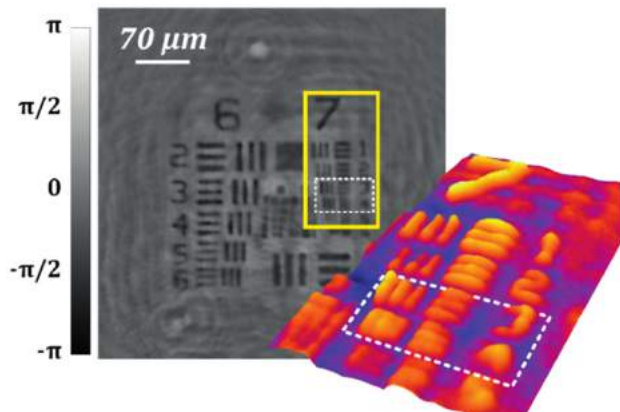


Fig. 7. Phase reconstruction of a pure-phase USAF 1951 target. The accompanying inset shows a 3D representation of the yellow-bounded region of group 7. The test shows a resolution capability between 2.76 and $3.10\text{ }\mu\text{m}$.

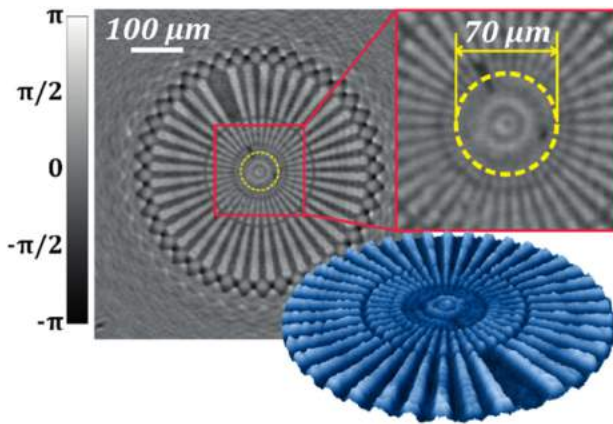


Fig. 8. Phase reconstruction of a pure-phase star test target. The dashed yellow line marks the minimum resolvable circumference, which, for this 40-spoke test, sets the resolution limit at $2.75 \mu\text{m}$.

and thus fulfilling the weak scattering condition [25]. Initially, the system was configured with an illumination distance of 10.56 mm, measured from the point source to the digital camera; placing the USAF-1951 resolution target 2.36 mm away from the source of spherical wavefronts, two recordings were made: the hologram and its associated reference as previously described. Figure 7 shows the corresponding phase reconstruction, in which all the features up to element 3 of group 7 can be fully resolved, while element 4 of this same group is only partially resolved. These observations are further supported by the

3D-height profile calculated over the yellow-bounded region of group 7; despite the phase irregularities inherited from the twin-image presence and some coherent noise, the reconstructed image produces an overall good recreation of the USAF-1951 features. From the resolved elements, the resolution capability of the recording geometry can be expected to lie between 2.76 and $3.10 \mu\text{m}$.

Similar results are achieved using the star test target while keeping the same illumination distance of 10.56 mm and a point-source-to-sample distance of 2.36 mm. Figure 8 shows the phase reconstruction obtained by the described two-shot experimental procedure. Once again, despite the unavoidable phase distortions, the results show high reconstruction quality and fidelity to the morphology of the sample. According to the manufacturer's information, the employed target has a 400 μm external diameter and 40 identical spokes; therefore, the smallest resolvable circumference, marked by the yellow dashed circle that has a 70 μm diameter, sets the resolution limit for the recording geometry at approximately $2.75 \mu\text{m}$, which is consistent with the previous result on the USAF-1951 test.

Finally, if a uniform refraction index of 1.52 is assumed for both samples; as reported by the manufacturer of the target, the average phase delays introduced by the USAF 1951 and the star test correspond to an estimated height of 378 nm and 156 nm, respectively. These values, measured over the features of each test against the mean background value, are in agreement with the nominal values of 350 nm and 150 nm.

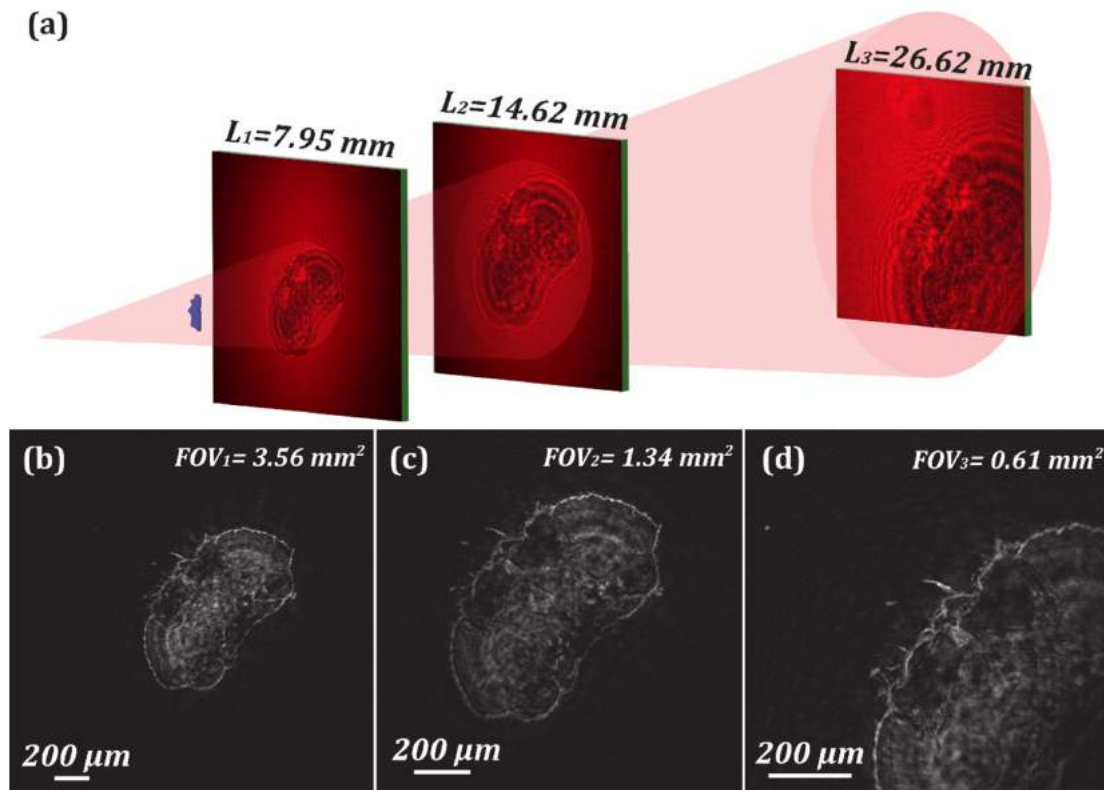


Fig. 9. Intensity reconstructions of a thin section of the head from a *Drosophila melanogaster* fly with different field of view values. (a) Hologram recording setup for three camera positions and, thus, variable illumination distances. (b),(c),(d) Intensity reconstruction for illumination distances of 7.95, 16.62, and 26.62 mm, respectively.

B. Field of View

To test the constructed microscope capability of adjusting the available FOV and achieving different magnifications of the diffraction pattern, a thin section of the head of a *Drosophila melanogaster* fly has been imaged at different camera positions. Following the description in Eq. (6), by modifying the distance between the sample and the camera, different values of FOV are obtained. Panel (a) of Fig. 9 shows three example positions of the sensor and the hologram that is registered at each illumination distance. Panels (b), (c), and (d) of the same figure show the intensity reconstructions for these three positions, corresponding to illumination distances of 7.95, 14.62, and 26.62 mm, respectively. Each panel, and thus each camera position, has an increasing diffraction pattern magnification due to the larger propagation distance; consequently, as the sensor remains the same size, there is a reduction of the FOV, namely, 3.56, 1.34, and 0.61 mm² are obtained for the three considered positions in the same order as before.

C. Common Biological Specimens

As a final usability verification of the open-source, cost-effective, 3D-printed DLHM, two biological samples of common interest were imaged, namely, buccal cells and human blood cells. To demonstrate the label-free imaging capabilities of DLHM over micrometric translucent objects [24,25], these samples were subjected to neither a special preparation process nor any sort staining.

Initially, the microscope was configured with the point source at a distance of 22.51 mm to the camera, and the sample was placed approximately 3 mm away from the source; these specifications set the observable FOV at 0.25 mm² and a maximum

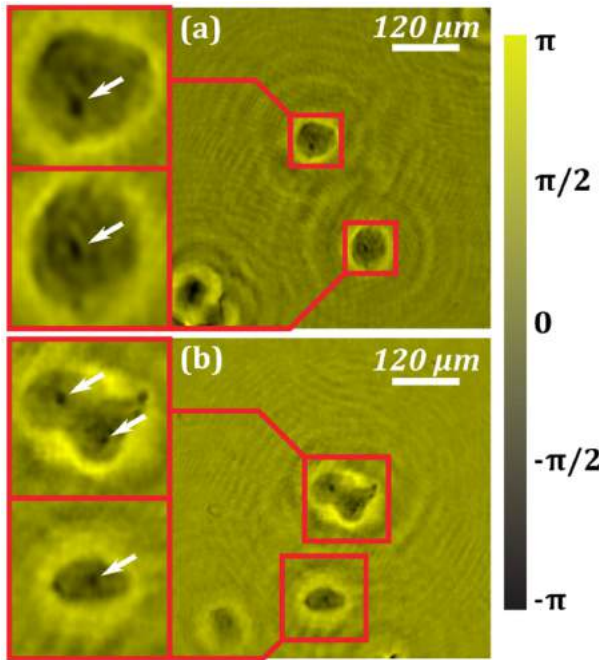


Fig. 10. Phase reconstructions from two different regions of an unstained buccal swab sample. The white arrows in the insets mark the nucleus position of each cell. The color scale bar applies to phase values in both panels.

resolution of 3.3 μm, allowing the effortless visualization of the buccal cells, whose transversal size is typically between 50 and 60 μm. With this configuration, a freshly taken buccal swab sample was imaged in two different regions using the two-shot procedure described at the beginning of this section. The resulting phase reconstructions are shown in Fig. 10, with each panel representing one of the imaged regions. The insets of both panels allow the observation of fine inner details in the cells, including their nuclei as marked by the white arrows.

The illumination distance was then changed to 7.18 mm, and the human blood smear sample was placed as close as possible to the point source to observe the unstained blood cells. Figure 11 summarizes the resulting reconstructions in intensity and phase, taken from two different regions of the sample that were imaged using the aforementioned two-shot procedure. In panel (a), the intensity reconstruction of the first region is shown, containing two red blood cells. The FOV in this reconstruction is wide enough to allow the easy visualization of the erythrocytes, which are magnified in the accompanying insets. Panel (b) shows the phase reconstruction of a second region of the human blood smear sample, clearly including an erythrocyte and a neutrophil. These two specimens can be further inspected in the 3D renders included as insets of this last panel. Of special interest is the

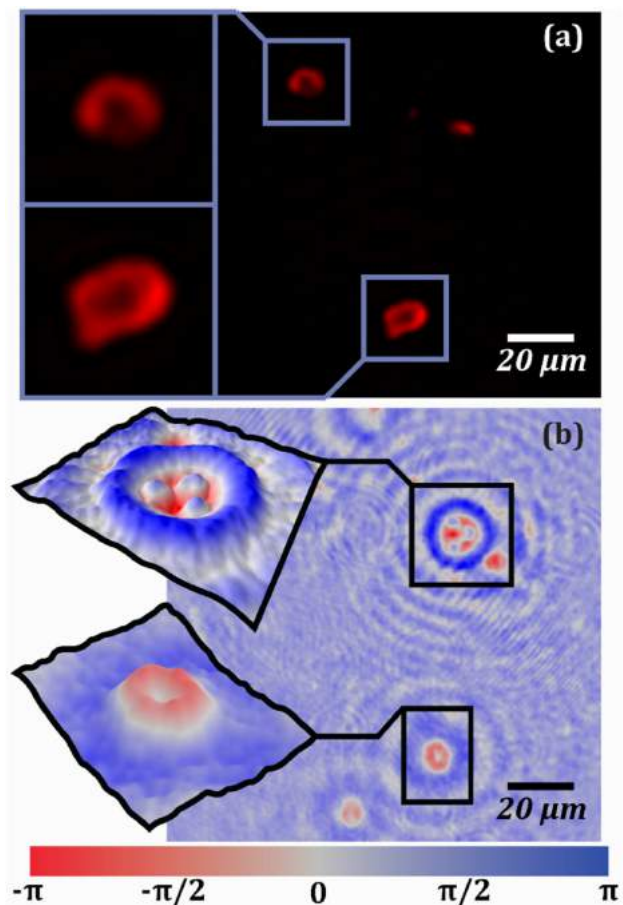


Fig. 11. Reconstruction of an unstained human blood smear sample. (a) Intensity reconstruction of erythrocytes. (b) Phase reconstruction, in a different region of the sample, showing an erythrocyte and a neutrophil.

neutrocyte, whose characteristic multisegmented nucleus can be seen in both the phase map and the 3D plot.

The results in both Figs. 10 and 11 portray the ability of the open-source, cost-effective, 3D-printed DLHM to achieve trustable visualizations of microscopic objects and biological specimens without any special sample preparation nor labeling process. The high quality of the experimental results and the versatility of the designed and constructed system position the proposed microscope as the most cost-effective digital lensless holographic microscope to date with proven applicability to common interest areas of DLHM.

5. CONCLUSIONS

The design, construction, and testing of the most cost-effective digital lensless holographic microscope to date have been presented. For digital lensless holographic microscopy (DLHM) to work, a point source produces spherical wavefronts that illuminate a sample placed close to the said point source. The diffracted wavefield propagates through the free space to reach a digital camera. The distance between the sample and the digital camera is set in such a way that the free-space propagation guarantees the magnification of the diffracted wavefield to be correctly recorded in the digital camera. The only needed hardware in DLHM is, therefore, a point source and a digital camera. To make the most cost-effective DLHM microscope up to date, the design and building of the body of the microscope via an optimized 3D-printable model have been presented; the said design and building encompass all the needed degrees of freedom to achieve a DLHM setup with variable FOV and spatial resolution that can be utilized in different applications. All the CAD files for the 3D printing and the list of materials with a supplier company will be fully available by request to the authors. The point source has been made by coupling a US\$1.03 laser diode to a US\$4.70 aspherical lens. This simple setup produces an illuminating point source with a numerical aperture (NA) of 0.65; with this NA at the 650 nm operating wavelength, a maximum theoretical spatial resolution of 500 nm can be achieved. For the recording of the in-line holograms, a surveillance digital camera costing US\$43.40 is utilized. The 3D printing of the DLHM microscope body and the slide holder needs, approximately, 102 grams of polylactic acid (PLA), which costs around US\$1.60. For the assembly and operation of the DLHM microscope, 20 screws are needed with a joint cost of US\$1.00. The former values set an overall price for the materials needed to build the cost-effective DLHM microscope presented in this work at just US\$52.82, which thus renders this design the most cost-effective DLHM microscope to date. Optimized software for the recording and processing of the in-line holograms has also been made available in an open-source philosophy, to set up a complete platform of DLHM accessible for everyone, with a special focus on low-resource settings. The proposed platform embraces the state-of-art technology available of DLHM with variable spatial resolutions reaching the micrometer-sized range and FOVs ranging from 0.023 to 11.2 mm².

The cost-effective state-of-the-art DLHM microscope has been tested on imaging pure phase resolution test targets and a *Drosophila melanogaster* head section in phase and intensity, respectively, showing its feasibility on the two modalities of

any digital holographic approach to microscopy and evaluating its spatial resolution and variable FOV. Additionally, to show its usability in traditional microscopy imaging applications, human blood cells and buccal cells were imaged; these samples were used without special preparations nor staining, proving the label-free capabilities of DLHM in the designed and constructed system. While the constructed version of the microscope could not reach full-range access to the design parameters, the results support the claimed micrometer-sized spatial resolution and the variable FOV achievable with the US\$52.82 DLHM microscope while maintaining high-quality reconstructions of microscopic objects and even pure phase ones.

The presented development of this DLHM microscope shows great promise as a disposable state-of-the-art microscopy tool to be used in remote areas as a point-of-care diagnosis tool, as a teaching tool for modern technologies of microscopy, and/or as a research tool for laboratories with limited resources.

Funding. Universidad Nacional de Colombia (Hermes 49282, Hermes 50210).

Acknowledgment. The authors of this paper acknowledge all the former and present members of the Optics and Opto-digital Processing Group of the Universidad Nacional de Colombia Sede Medellin who have historically contributed to the development of the extremely cost-effective DLHM microscope presented in this work.

Disclosures. The authors declare no conflicts of interest.

REFERENCES

1. J. T. Collins, J. Knapper, J. Stirling, J. Mduda, C. Mkindi, V. Mayagaya, G. A. Mwakajinga, P. T. Nyakyi, V. L. Sanga, D. Carbery, L. White, S. Dale, Z. J. Lim, J. J. Baumberg, P. Cicuta, S. McDermott, B. Vodenicharski, and R. Bowman, "Robotic microscopy for everyone: the openflexure microscope," *Biomed. Opt. Express* **11**, 2447–2460 (2020).
2. E. Cuche, F. Bevilacqua, and C. Depeursinge, "Digital holography for quantitative phase-contrast imaging," *Opt. Lett.* **24**, 291–293 (1999).
3. E. Cuche, P. Marquet, and C. Depeursinge, "Simultaneous amplitude-contrast and quantitative phase-contrast microscopy by numerical reconstruction of Fresnel off-axis holograms," *Appl. Opt.* **38**, 6994–7001 (1999).
4. M. Takeda, H. Ina, and S. Kobayashi, "Fourier-transform method of fringe-pattern analysis for computer-based topography and interferometry," *J. Opt. Soc. Am.* **72**, 156–160 (1982).
5. E. Cuche, P. Marquet, and C. Depeursinge, "Spatial filtering for zero-order and twin-image elimination in digital off-axis holography," *Appl. Opt.* **39**, 4070–4075 (2000).
6. J. K. Wallace, S. Rider, E. Serabyn, J. Kühn, K. Liewer, J. Deming, G. Showalter, C. Lindensmith, and J. Nadeau, "Robust, compact implementation of an off-axis digital holographic microscope," *Opt. Express* **23**, 17367–17378 (2015).
7. T. Beckmann, M. Fratz, A. Schiller, A. Bertz, and D. Carl, "Digital holographic microscopy for 200 € using open-source hard- and software," in *Opt. InfoBase Conf.* (2019), pp. 7–8.
8. M. Rostykuš and C. Moser, "Compact lensless off-axis transmission digital holographic microscope," *Opt. Express* **25**, 16652–16659 (2017).

9. S. Rawat, S. Komatsu, A. Markman, A. Anand, and B. Javidi, "Compact and field-portable 3D printed shearing digital holographic microscope for automated cell identification," *Appl. Opt.* **56**, D127–D133 (2017).
10. T. O'Connor, A. Doblas, and B. Javidi, "Structured illumination in compact and field-portable 3D-printed shearing digital holographic microscopy for resolution enhancement," *Opt. Lett.* **44**, 2326–2329 (2019).
11. T. Cacace, V. Bianco, B. Mandracchia, V. Pagliarulo, E. Oleandro, M. Paturzo, and P. Ferraro, "Compact off-axis holographic slide microscope: design guidelines," *Biomed. Opt. Express* **11**, 2511–2532 (2020).
12. M. K. Kim, *Digital Holographic Microscopy: Principles, Techniques, and Applications* (Springer, 2011).
13. O. Mudanyali, D. Tseng, C. Oh, S. O. Isikman, I. Sencan, W. Bishara, C. Oztoprak, S. Seo, B. Khademhosseini, and A. Ozcan, "Compact, light-weight and cost-effective microscope based on lensless incoherent holography for telemedicine applications," *Lab Chip* **10**, 1417–1428 (2010).
14. D. Tseng, O. Mudanyali, C. Oztoprak, S. O. Isikman, I. Sencan, O. Yaglidere, and A. Ozcan, "Lensfree microscopy on a cellphone," *Lab Chip* **10**, 1787–1792 (2010).
15. M. Lee, O. Yaglidere, and A. Ozcan, "Field-portable reflection and transmission microscopy based on lensless holography," *Biomed. Opt. Express* **2**, 2721–2730 (2011).
16. E. McLeod and A. Ozcan, "Microscopy without lenses," *Phys. Today* **70**, 50–56 (2017).
17. T. G. Dimiduk, E. A. Kosheleva, D. Kaz, R. McGorty, E. J. Gardel, and V. N. Manoharan, "A simple, inexpensive holographic microscope," in *Biomedical Optics and 3-D Imaging*, OSA Technical Digest (CD) (Optical Society of America, 2010), paper JMA38.
18. T. Shimobaba, Y. Taniguchi, A. Shiraki, N. Masuda, and T. Ito, *Portable and low-cost digital holographic microscopy using web camera, point light source LED and open-source libraries* (2012), paper JM3A.50.
19. M. Sanz, J. Á. Picazo-Bueno, L. Granero, J. Garcíá, and V. Micó, "Compact, cost-effective and field-portable microscope prototype based on MISHELF microscopy," *Sci. Rep.* **7**, 43291 (2017).
20. M. Sanz, M. Trusia, J. García, and V. Micó, "Variable zoom digital in-line holographic microscopy," *Opt. Laser Eng.* **127**, 105939 (2020).
21. S. Amann, M. von Witzleben, and S. Breuer, "Open-source 3D-printed digital inline holographic microscope for low-cost cellular imaging," *Proc. SPIE* **11306**, 113060B (2020).
22. H. J. Kreuzer, H. W. Fink, H. Schmid, and S. Bonev, "Holography of holes, with electrons and photons," *J. Microsc.* **178**, 191–197 (1995).
23. W. Xu, M. H. Jericho, I. A. Meinertzhausen, and H. J. Kreuzer, "Digital in-line holography for biological applications," *Proc. Natl. Acad. Sci. USA* **98**, 11301–11305 (2001).
24. J. Garcia-Sucerquia, W. Xu, S. K. Jericho, P. Klages, M. H. Jericho, and H. J. Kreuzer, "Digital in-line holographic microscopy," *Appl. Opt.* **45**, 836–850 (2006).
25. D. Gabor, "A new microscopic principle," *Nature* **161**, 777–778 (1948).
26. J. W. Goodman, *Introduction to Fourier Optics*, 3rd ed. (Roberts & Company, 2005).
27. S. K. K. Jericho, J. Garcia-Sucerquia, W. Xu, M. H. H. Jericho, and H. J. J. Kreuzer, "Submersible digital in-line holographic microscope," *Rev. Sci. Instrum.* **77**, 043706 (2006).
28. S. Seo, T. W. Su, A. Erlinger, and A. Ozcan, "Multi-color LUCAS: Lensfree on-chip cytometry using tunable monochromatic illumination and digital noise reduction," *Cell. Mol. Bioeng.* **1**, 146–156 (2008).
29. S. Seo, T.-W. Su, D. K. Tseng, A. Erlinger, and A. Ozcan, "Lensfree holographic imaging for on-chip cytometry and diagnostics," *Lab Chip* **9**, 777–787 (2009).
30. W. Bishara, T.-W. Su, A. F. Coskun, and A. Ozcan, "Lensfree on-chip microscopy over a wide field-of-view using pixel super-resolution," *Opt. Express* **18**, 11181–11191 (2010).
31. M. Sanz, J. A. Picazo-Bueno, J. García, and V. Micó, "Improved quantitative phase imaging in lensless microscopy by single-shot multi-wavelength illumination using a fast convergence algorithm," *Opt. Express* **23**, 21352–21365 (2015).
32. M. Sanz, J. Á. Picazo-Bueno, L. Granero, J. García, and V. Micó, "Multi-illumination single-holographic-exposure lensless Fresnel (MISHELF) microscopy using 4 channels," in *Imaging and Applied Optics (COSI, IS, MATH, PcaOP)*, OSA Technical Digest (Optical Society of America, 2019), paper JW2A.1.
33. J. Garcia-Sucerquia, "Color lensless digital holographic microscopy with micrometer resolution," *Opt. Lett.* **37**, 1724–1726 (2012).
34. B. Patiño-Jurado, J. F. Botero-Cadavid, and J. Garcia-Sucerquia, "Cone-shaped optical fiber tip for cost-effective digital lensless holographic microscopy," *Appl. Opt.* **59**, 2969–2975 (2020).
35. M. H. Jericho and H. J. Kreuzer, "Point source digital in-line holographic microscopy," in *Coherent Light Microscopy*, P. Ferraro, A. Wax, and Z. Zalevsky, eds. (Springer-Verlag, 2011), pp. 3–30.
36. C. Trujillo, P. Piedrahita-Quintero, and J. Garcia-Sucerquia, "Digital lensless holographic microscopy: numerical simulation and reconstruction with ImageJ," *Appl. Opt.* **59**, 5788–5795 (2020).
37. J. Garcia-Sucerquia, D. C. Alvarez-Palacio, and H. J. Kreuzer, "High resolution Talbot self-imaging applied to structural characterization of self-assembled monolayers of microspheres," *Appl. Opt.* **47**, 4723–4728 (2008).
38. M. Kanka, R. Riesenbergs, P. Petrucc, and C. Graulig, "High resolution (NA=0.8) in lensless in-line holographic microscopy with glass sample carriers," *Opt. Lett.* **36**, 3651–3653 (2011).
39. P. Petrucc, R. Riesenbergs, and R. Kowarschik, "Optimized coherence parameters for high-resolution holographic microscopy," *Appl. Phys. B* **106**, 339–348 (2012).
40. V. Micó and Z. Zalevsky, "Superresolved digital in-line holographic microscopy for high-resolution lensless biological imaging," *J. Biomed. Opt.* **15**, 046027 (2010).
41. J. Garcia-Sucerquia, W. Xu, S. K. K. Jericho, M. H. H. Jericho, P. Klages, and H. J. J. Kreuzer, "Resolution power in digital in-line holography," *Proc. SPIE* **6027**, 60272H (2006).
42. B. Patiño-Jurado, J. F. Botero-Cadavid, and J. Garcia-Sucerquia, "Step-index optical fibers with 0.88 numerical aperture," *J. Lightwave Technol.* **37**, 3734–3739 (2019).
43. B. Patiño-Jurado, J. F. Botero-Cadavid, and J. Garcia-Sucerquia, "Optical fiber point-source for digital lensless holographic microscopy," *J. Lightwave Technol.* **37**, 5660–5666 (2019).
44. E. E. Te Hwu and A. Boisen, "Hacking CD/DVD/Blu-ray for biosensing," *ACS Sens.* **3**, 1222–1232 (2018).
45. E. Serabyn, K. Liewer, C. Lindensmith, K. Wallace, and J. Nadeau, "Compact, lensless digital holographic microscope for remote microbiology," *Opt. Express* **24**, 28540–28548 (2016).
46. L. Mandel, E. Wolf, and P. Meystre, "Optical coherence and quantum optics," *Am. J. Phys.* **64**, 1438 (1996).
47. C. A. Schneider, W. S. Rasband, and K. W. Eliceiri, "NIH image to ImageJ: 25 years of image analysis," *Nat. Methods* **9**, 671–675 (2012).